ACS APPLIED MATERIALS & INTERFACES

Research Article

www.acsami.org

Enhanced Supercapacitor Performance of Mn_3O_4 Nanocrystals by Doping Transition-Metal Ions

Ruiting Dong, Qinglan Ye, Lili Kuang, Xu Lu, Ying Zhang, Xue Zhang, Guojin Tan, Yanxuan Wen, and Fan Wang*

School of Chemistry and Chemical Engineering, Guangxi University, Nanning 530004, P. R. China

Supporting Information

ABSTRACT: Pristine and transition-metal-doped Mn_3O_4 nanocrystals shaped in octahedrons have been synthesized by hydrothermal reduction of potassium permanganate and characterized by SEM/TEM, X-ray diffraction, X-ray photoelectron spectroscopy, and electrochemical experiments. The results reveal that a multistep reduction process is taking place, and the introduction of doping ions causes a direct synthesis of single-phase Mn_3O_4 nanocrystals. To assess the properties of Mn_3O_4 nanocrystals for their use in supercapacitors, cyclic voltammetry and galvanostatic charging−discharging measurements are performed. The phase stability during cycling and charge-transfer behavior are greatly improved by doping with transition metal, and Cr-doped Mn_3O_4 nanocrystals exhibit a maximum specific capacitance of 272 F g^{-1} at a current density of 0.5 A g^{-1}. These doped Mn_3O_4 nanocrystals could be a promising candidate material for high-capacity, low-cost, and environmentally friendly electrodes for supercapacitors. In addition, these results have verified the ability of doping to improve capacitive performances of spinel-structured transition-metal oxides.

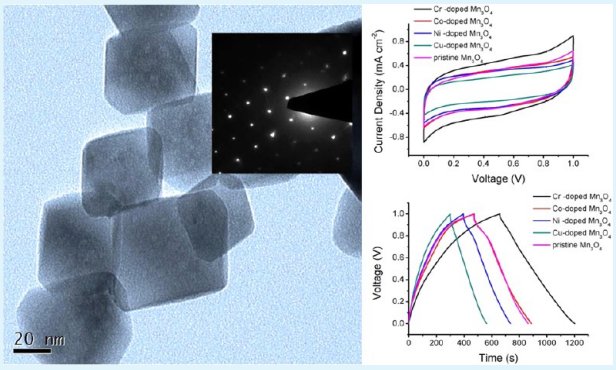

KEYWORDS: *Mn oxides, doping, supercapacitors, phase stability*

1. INTRODUCTION

Supercapacitors (SCs) represent a new type of energy storage device that have the advantages of high power density, environmental friendliness, high safety, and convenient operation over a wide temperature range, and they show tremendous flexibility in complementing lithium-ion batteries. On the basis of their energy storage mechanism, SCs can be categorized into electric double-layer capacitors (EDLCs) and pseudocapacitors.[1] For EDLCs, the energy storage is based on the adsorption of ions and the orientation of polar solvent molecules or ions at the electrode/electrolyte interfaces in which the accumulation of electrons at the electrode is a nonfaradaic process. The EDLCs using porous carbon materials have an excellent cyclic stability and a long service lifetime. However, their capacitance (typically in the range of 75−175 F g^{-1}) is restricted by the specific surface area and the pore-size distribution.[2] Hence, most current research work on SCs has been focused on pseudocapacitors to improve their energy density and make them comparable to Li batteries. Pseudocapacitance is originated from the fast and reversible faradaic reaction of the electrode material with the electrolyte. The electrons produced by the faradaic reaction are transferred across the electrolyte/electrode interface, resulting in current passing through the cell. Because of the high theoretical capacitance of ∼1370 F g^{-1}, Mn-based oxide has been one of the most promising electrode materials for SCs. For MnO_2, the piling up of $[MnO_6]$ octahedral enables the building of 1D tunnel structures and layers of various sizes. Generally, MnO_2 electrodes with a larger tunnel favored the storage of alkaline cations (e.g., Na^+, K^+, and Li^+) and exhibited higher capacitance.[3−5] Ghodbane et al. demonstrated the structure-dependent charge storage mechanisms of Mn oxides.[6] However, because of the structural complexity of Mn(IV) oxides, the relationships between microstructures and electrochemical performances are sometimes conflicting. On the other hand, the mixed-valent Mn oxides also show high specific capacitance, which is a good candidate for electrode material toward SCs.[7] Mixed-valent spinel Mn_3O_4 has attracted significant interest because of its potential applications in catalysis, rechargeable lithium-ion batteries, molecular adsorption, and gas sensing. In particular, the tunable capacitive behavior of Mn_3O_4 nanostructures have been investigated.[8−10] Nevertheless, the poor electrical intrinsic conductivity of Mn_3O_4 materials also severely affects their capacity. The fabrication of a graphene−metal oxide hybrid nanostructure is a facile way to promote the rate performance of electrode materials with low conductivity.[11−16] Unfortunately, it did not demonstrate a large rise in its capacity value at a low charge−

Received: June 10, 2013
Accepted: September 3, 2013
Published: September 3, 2013

discharge current density. Mn oxides with high capacity are still needed to maximize the electrochemical performance of a competitive supercapacitor.

To maximize Mn oxide for electrochemical utilization, a series of alkali metal-ion intercalation-layered Mn compounds were synthesized to improve the diffusion performance of electrotype ions in an electrode's solid phase.[17,18] The enhancement in electrochemical activity indicated an effective preintercalation effect. However, for a spinel-structure compound, it is still unclear if the preintercalation effect will work.[19,20] Doping with transition-metal ions is another frequently employed method to modify the properties of functional materials. Because of the confinement of electronic states and the tendency to occupy the sites in the crystalline structure, doping Mn-based nanostructures may be inducing new phenomena not found in bulk materials. For instance, cationic doping using 3d transition metals have been adopted to stabilize the spinel $LiNi_{0.5}Mn_{1.5}O_4$ structure and eliminate the impurity phase.[21] Also, doping is a powerful way to enhance the intrinsic conductivity of Mn oxide as well as to improve the capacitive performance of Mn oxides electrodes.[22] However, few reports have been published regarding transition-metal doping into Mn_3O_4. In this work, we propose a hydrothermal approach to incorporate a 3d transition metal into Mn_3O_4 nanocrystals. The effects of metal doping on crystal growth, morphology, and electrochemical properties of Mn_3O_4 nanocrystals are investigated. The results provide clear evidence that metal doping can promote the formation of single-phase Mn_3O_4 by preventing the presence of the MnOOH phase and effectively improve the capacitive performance, which may be provide new insights into establishing a doping model in SCs.

2. EXPERIMENTAL METHODS

All of the reagents were of analytical grade and used as received without any further purification.

2.1. Synthesis. In a typical synthetic procedure to obtain doped Mn_3O_4 nanocrystals, 2.4 mmol of $KMnO_4$ was dissolved in 20 mL of deionized water at room temperature. Then, 0.46 mmol of glucose, a nontoxic and mild reducing agent, was gradually added into the solution while stirring vigorously. The resultant brown suspension was stirred for 10 min. The doping metal (Cr^{3+}, Co^{2+}, Ni^{2+}, and Cu^{2+}) sulfates were introduced into the solution, with a molar ratio of doping metal to Mn of 0.05. The mixture was stirred for another 30 min and then transferred into a 25 mL capacity Teflon-lined autoclave and maintained at 200 °C for 2 h. After the hydrothermal process, the autoclave was allowed to cool naturally. The resulting solid product was filtered, washed with distilled water and absolute ethanol, and finally dried at 60 °C for 6 h.

2.2. Characterization. The structural phases of the products were measured by powder X-ray diffraction (XRD) experiments on a RigaKu D/max-RB diffractometer with Cu Kα radiation. A scanning electron microscopy system (SEM, S-3400N, Hitachi) was used to observe the morphology of the doped Mn_3O_4 nanocrystals. A transmission electron microscopy system (TEM, JEM-2010, JEOL) with a 200 kV acceleration voltage was used to obtain the structural information of the products. X-ray photoelectron spectroscopy (XPS, Axis Ultra, Kratos) was used to establish the valence states of Mn in the products. To correct for possible charging of the materials by the X-ray irradiation, the binding energy was calibrated using the C 1s (284.8 eV) spectrum for the hydrocarbon that remained in the XPS analysis chamber as a contaminant.

2.3. Electrode Preparation and Electrochemical Experiment. To fabricate working electrodes, the prepared Mn oxide material (75 wt %), acetylene black (20 wt %), and poly(vinylidene) fluoride binder (5 wt %) were mixed. A homogeneous slurry of the above mixture was made using *N*-methyl-2-pyrrolidone as a solvent. The slurry was subsequently brush-coated onto Ni mesh. The mesh was dried at 60 °C in air for 8 h for the removal of the solvent. Each composite electrode contained 0.3 mg of electro-active material and had a geometric surface area of about 1 cm^2. A typical three-electrode glass cell equipped with a working electrode, a platinum foil counter electrode, and a Ag/AgCl reference electrode was used for electrochemical measurements. Cyclic voltammetry (CV) and galvanostatic charge−discharge measurements were performed using an electrochemical workstation (CHI660D, Shanghai, China) in a 1 M Na_2SO_4 aqueous solution. Electrochemical impedance spectroscopy (EIS) was conducted by sweeping frequencies from 1 mHz to 100 kHz. The measured impendence data were analyzed using the ZSimpWin program. Before the electrochemical tests, the working electrodes were aged for 12 h to ensure good soakage of the active material in the electrolyte.

3. RESULTS AND DISCUSSION

A complete understanding of the formation of Mn_3O_4 nanocrystals without any dopant is necessary to know the determinant influences of the reductant on the crystalline structure of manganese oxide. The XRD patterns of the reduced products of $KMnO_4$ by glucose are shown in Figure 1.

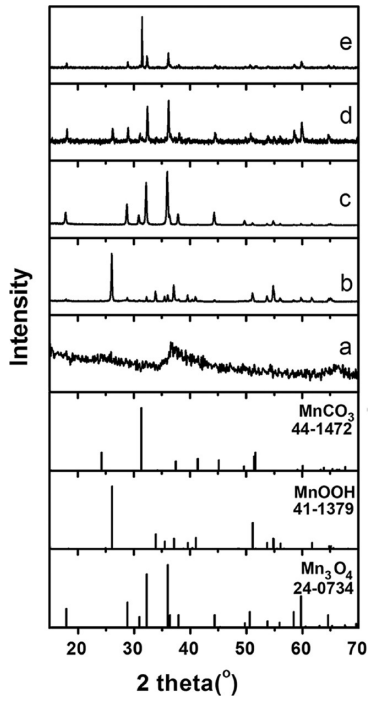

Figure 1. XRD patterns of the reduced products of $KMnO_4$ by glucose. Precipitate prepared at room temperature (a) and hydrothermal products obtained at 140 °C for 2 h (b), 140 °C for 24 h (c), 200 °C for 2 h (d), and 200 °C for 24 h (e).

The precipitate prepared at room temperature shows an amorphous Mn oxide having peaks indexing to an α-MnO_2 structure, suggesting a fast redox reaction between $KMnO_4$ and glucose at room temperature (Figure 1a). There is an increase in crystallinity with respect to the increase of the hydrothermal dwell time, as evidenced by the appearance of sharp peaks. At 140 °C for 2 h, the two phases of MnOOH (JCPDS 41-1379) and Mn_3O_4 (JCPDS 80-0382) have both been confirmed in the XRD patterns with the main phase of MnOOH (Figure 1b). An elongated reaction time of 24 h at 140 °C leads to the formation of the pure Mn_3O_4 phase, as shown in Figure 1c. The possible process may be a multistep reduction reaction. That is,

Mn^{3+} or MnOOH is formed first by reduction of MnO_2 under hydrothermal conditions. Glucose is a hydroxyl-enriched molecule, and plenty of −OH groups would be available to facilitate the formation of MnOOH and prevent the transformation of MnOOH to Mn_2O_3. Next, Mn^{2+} is partially formed by further reduction, and Mn_3O_4 is achieved. This reaction is accelerated at relatively high temperatures. When the temperature is raised to 200 °C, the mixture of MnOOH and Mn_3O_4 is still achieved after 2 h of the hydrothermal reaction, whereas the main phase changes to Mn_3O_4 (Figure 1d). Hence, the single-phase nature of resultant manganese oxides (MnOOH or Mn_3O_4) is effectively controlled by tuning the reaction time and temperature in a hydrothermal route. However, an extension of the reaction time to 24 h at 200 °C leads to the formation of the $MnCO_3$ structure as a main phase (Figure 1e). The generation of $MnCO_3$ is mainly due to the deep oxidation of glucose by $KMnO_4$.

Under the hydrothermal environment, the formation of single-crystalline Mn_3O_4 is favored with the coexistence of Mn^{2+} and Mn^{3+} in the solution. By ionic replacement, a direct synthesis of single-phase Mn_3O_4 may occur with the introduction of doping ions into the precursor solution. The XRD patterns of the doped Mn_3O_4 synthesized at 200 °C for 2 h are shown in Figure 2. The patterns of four doped samples fit

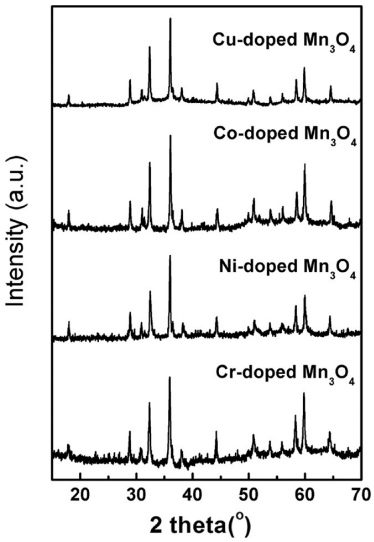

Figure 2. XRD patterns of the doped Mn_3O_4 synthesized at 200 °C for 2 h.

basically to the spinel Mn_3O_4 structure, and the phases of doped metal oxide are not detected, indicating the effectiveness of doping in eliminating the MnOOH phase. A comparison of the XRD patterns of pristine and doped Mn_3O_4 samples shows the shifts of the peak position toward higher 2θ angles for Co-, Ni-, and Cu-doped Mn_3O_4, and the shift toward a lower angle for Cr-doped Mn_3O_4, indicating the variation in the unit-cell volume expected from the substitution of the dopant ions for Mn ions in the Mn_3O_4 host (Supporting Information Figure S1). Hence, it is rational to assume that two types of effective lattice substitution of Mn ions by doping ions might be taking place depending on the matching of the oxidation state. The possible substitution of metal ions Co^{2+}, Ni^{2+}, and Cu^{2+} for Mn^{2+} in the tetrahedral sites is primarily due to the comparable ionic radii of Mn^{2+} (0.80 Å), Co^{2+} (0.74 Å), Ni^{2+} (0.69 Å), and Cu^{2+} (0.73 Å). A lattice substitution of Mn^{3+} in the octahedral sites by Cr^{3+} and a slight increase in cell volume are also expected because the ionic radii of Cr^{3+} (0.61 Å) is close to that of Mn^{3+} (0.58 Å). The additional peaks at 2θ of about 31.4° for Co-, Ni-, and Cu-doped samples are due to diffraction from the (104) plane of $MnCO_3$ (JCPDS 44-1472). For the Cr-doped sample, only the pure Mn_3O_4 phase is observed.

The XPS analysis is carried out to confirm the valence states of the Mn and dopants in the pristine and doped Mn_3O_4 samples. As shown in Figure 3, the characteristic binding energy

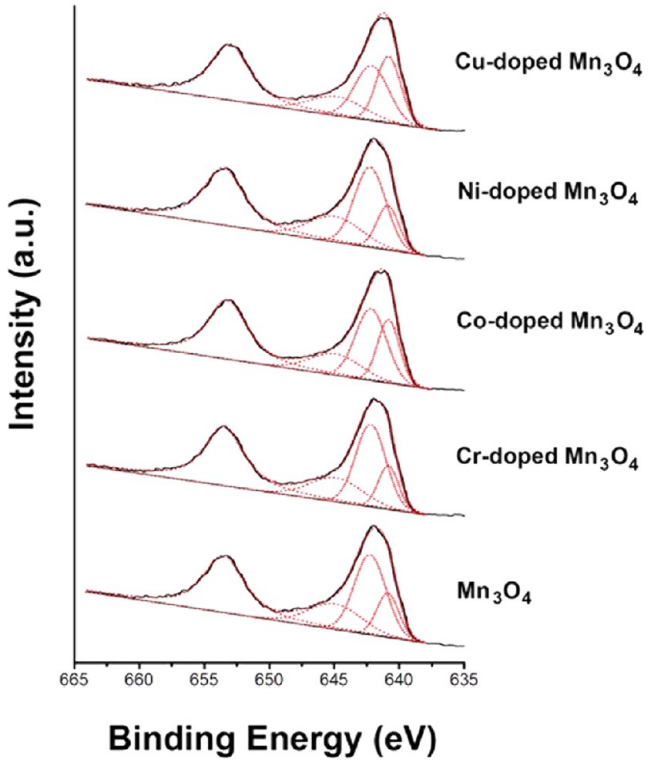

Figure 3. Mn 2p electron XPS spectra and its fitting curves for pristine and doped Mn_3O_4 product.

of unfitted Mn $2p_{3/2}$ peak for pristine Mn_3O_4 is 641.3 eV. This is in agreement with the data reported in previous work (with the Mn $2p_{3/2}$ peak situated at 641.3−641.5 eV).[23−27] The binding energies of Mn $2p_{3/2}$ have a ∼0.2 eV increase after Co doping and a ∼0.4 eV increase after Cr or Ni doping. Such a shift in binding energy, which is probably due to electron transfer between Mn_3O_4 and the dopants, suggests a strong interaction and competitive effect. Mn_3O_4 is a mixed valence oxide containing both Mn(II) and Mn(III) ions. Hence, the XPS spectrum of Mn_3O_4 has a larger doublet separation of the Mn $2p_{1/2}$ and Mn $2p_{3/2}$ spin orbit levels compared to the simple oxides because there is a weak interaction between the different ion sites. In this work, an energy separation of 11.9 eV between the Mn $2p_{1/2}$ and Mn $2p_{3/2}$ peaks can be found for pristine and doped Mn_3O_4 nanocrystals. To obtain further information about the actual metal oxidation state in the products, the XPS peaks were fitted using Gaussian functions to achieve the relative intensities of the component. The Mn $2p_{3/2}$ peaks can be fitted by three Gaussian functions. Two components of peak are centered at 640.8 and 642.2 eV, suggesting that the valence of the Mn ions is +2 and +3, respectively. However, the identification of various Mn ionic species present in the sample and the ability to obtain a

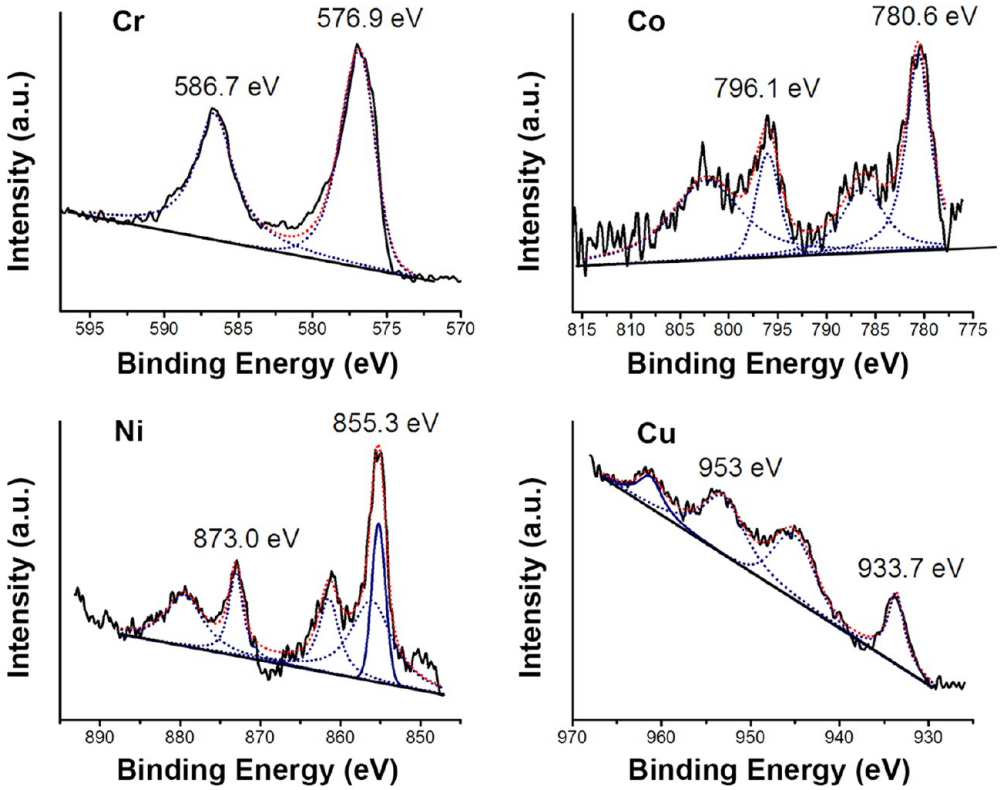

Figure 4. XPS spectra of Cr 2p, Co 2p, Ni 2p, and Cu 2p for each doped Mn_3O_4 product.

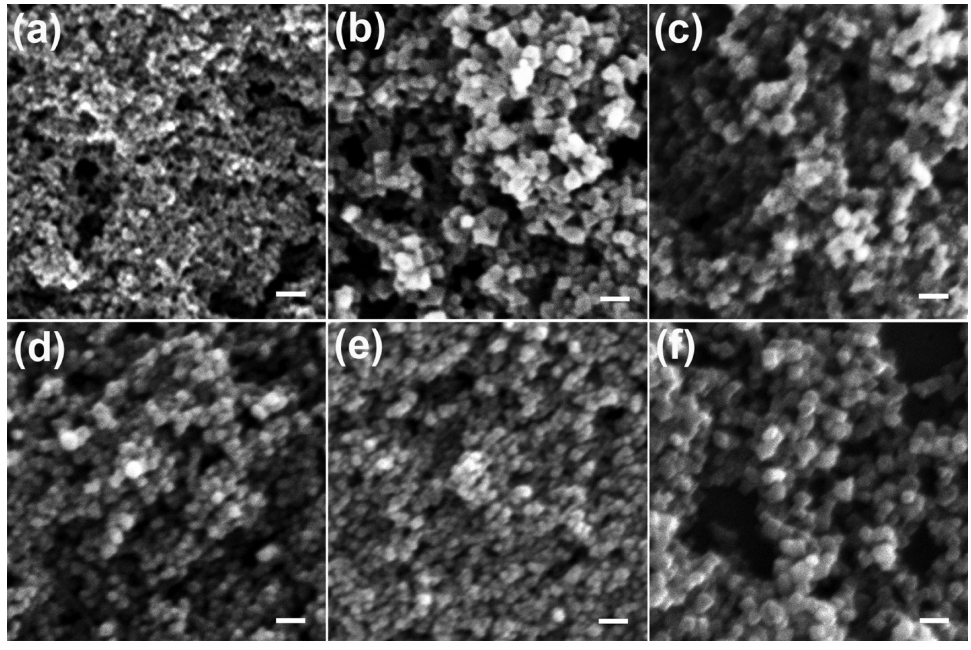

Figure 5. SEM images of the reduced products. Precipitate prepared at room temperature (a), pristine Mn_3O_4 (b), Cr-doped Mn_3O_4 (c), Co-doped Mn_3O_4 (d), Ni-doped Mn_3O_4 (e), and Cu-doped Mn_3O_4 (f). The scale bar is 200 nm.

consistent oxide composition is still difficult because of the similar binding energy of the Mn $2p_{3/2}$ peak components for Mn in the different oxidation states. The fitting line featured at 644.8 eV is the satellite peak of the Mn(II) $2p_{3/2}$ peak, which relates to the presence of the Mn(II) species. In fact, utilizing the XPS intensity ratio of the Mn $2p_{3/2}$ satellite to the main peak (abbreviated as the *c* value in this work) may reveal the valence change of Mn. For pristine Mn_3O_4, the *c* value equals about 0.32, which is characteristic of Mn_3O_4. The *c* values for doped Mn_3O_4 have respective changes. For Cr- and Ni-doped Mn_3O_4, the *c* values increase to about 0.35, revealing the high level of Mn(II) after doping. For Co-doped Mn_3O_4, the *c* value equals about 0.33, also indicating a slight content increase of Mn(II). Cu-doped Mn_3O_4 has the minimum *c* value (~0.29), suggesting a partial charge redistribution from Mn^{2+} to Mn^{3+} and the increasing average oxidation state of the Mn.

dx.doi.org/10.1021/am402257y | ACS Appl. Mater. Interfaces 2013, 5, 9508−9516

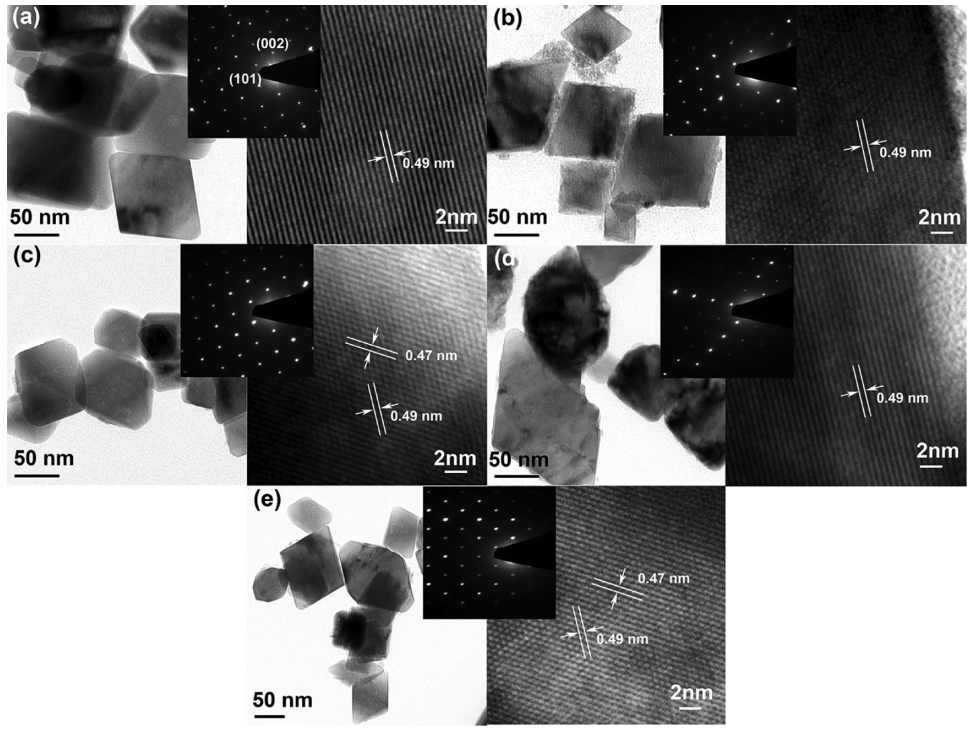

Figure 6. TEM and HRTEM images of pristine (a), Cr-doped (b), Co-doped (c), Ni-doped (d), and Cu-doped (e) Mn_3O_4 nanocrystals. The insets show the SAED patterns.

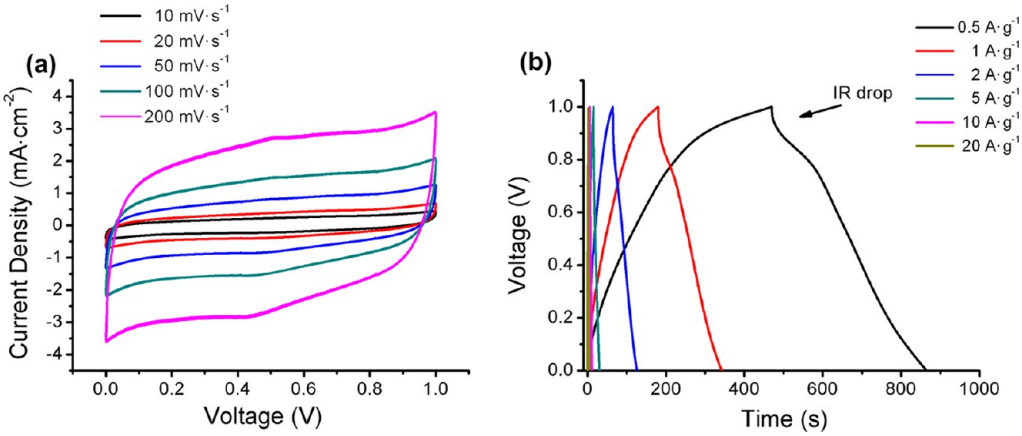

Figure 7. Electrochemical properties of pristine Mn_3O_4 nanocrystals. CV curves (a) and charge−discharge curves (b).

Figure 4 shows the binding energies of the doping metal 2p core levels. In the Cr region, two characteristic peaks for Cr $2p_{3/2}$ and Cr $2p_{1/2}$ at 576.9 and 586.7 eV are observed, and there is an energy separation of 9.6 eV between the Cr $2p_{1/2}$ and $2p_{3/2}$ peaks, which is characteristic of Cr^{3+} having the d^3 configuration.[28] In the Co region, the observed binding energies of cobalt $2p_{3/2}$ and $2p_{1/2}$ are 780.6 and 796.1 eV, respectively. However, the distinction between the oxidation states among many Co compounds is vague because the chemical shift of the main peaks of Co 2p electrons for Co^{2+} and Co^{3+} is not sufficiently obvious. The supposed binding energies of Co $2p_{3/2}$ are 780.4 ± 0.2 eV for CoO and 780.0 ± 0.2 eV for Co_3O_4. Nevertheless, the identical satellite structures apart from the main peaks and the Co $2p_{3/2}$−$2p_{1/2}$ spin−orbit splitting of 15.5 eV are evidence of Co^{2+} existence.[29−31] In the Ni region, two major components at 855.3 and 873.0 eV are attributed to Ni $2p_{3/2}$ and Ni $2p_{1/2}$, and each of them has a satellite. The Ni $2p_{3/2}$ spectra are fitted to two components. The signal at 854.8 eV assigned to Ni^{2+} ion is the main component of the Ni $2p_{3/2}$ peak. The peak at 856 eV is assigned to Ni^{3+} cations. The "shake up" satellite peak centered at 862 eV might be due to both types of Ni.[32] In the Cu region, the board peaks for Cu $2p_{3/2}$ and Cu $2p_{1/2}$ locate at 933.7 and 953 eV, respectively. A satellite peak at about 944 eV is observed, which is characteristic of a d^9 configuration of Cu^{2+} in the ground state. Hence, the oxidation states of transition-metal ions are still held after doping into Mn_3O_4 nanocrystals except for the Ni ion in which a partial oxidation arises.

Figure 5 shows the morphologies of the obtained Mn oxides. By mixing $KMnO_4$ and glucose at room temperature, Mn oxide particles with sizes of 20−40 nm are homogeneously formed (Figure 5a). After hydrothermal treatment at 200 °C, the pristine and doped Mn_3O_4 nanocrystals of tens of nanometers in size are clearly found in Figure 5b−f. To investigate further

the microstructure of the as-prepared nanocrystals, TEM imaging analysis was employed, as shown in Figure 6 and Supporting Information Figure S2. Pristine Mn_3O_4 nanocrystals are mostly faceted with an octahedral morphology, and the sizes range between 50 and 100 nm (Figure 6a). Octahedrons should be the thermodynamic equilibrium shapes of Mn_3O_4, which are determined by the surface energies of all of the facets and the intrinsic structure.[8,33] By doping with transition-metal ions, the Mn_3O_4 nanocrystals are changing in size, but they still keep an octahedron shape (Figure 6b–e). A decrease in the average rhombic length for Co- and Cu-doped nanocrystals and a slight increase for Cr- and Ni-doped nanocrystals are observed. There are a small amount of amorphous impurities in the Cr- and Ni-doped nanocrystals, which results in the partially covered and/or rude surface. In addition, two kinds of nano-octahedrons, regular octahedrons, and truncated octahedrons with small rectangular facets at the vertices are formed. Interestingly, the proportion of truncated octahedrons increases by doping with Co and Cu ions. For all five kinds of nanocrystals, the similar SAED patterns suggests the same growth behavior. The interplanar spacing of 0.49 and 0.47 nm in the HRTEM images corresponds to the interplane spacing of the (101) and (200) planes of Mn_3O_4, respectively. The EDX results of the doped nanocrystals indicate the existence of doping element in the samples (Supporting Information Figure S3).

The pristine and doped Mn_3O_4 nanocrystals were investigated as supercapacitor electrodes using cyclic voltammetry (CV) in a 1 M Na_2SO_4 aqueous solution with a three-electrode system. Representative CV curves of pristine Mn_3O_4 nanocrystals electrode over a range of scan rates from 10 to 200 mV s^{-1} are shown in Figure 7a. The CV curves exhibit nearly symmetrical shapes at a low scan rate, revealing the kinetic reversibility of the redox process as well as the ideal capacitive behaviors. The galvanostatic charge–discharge measurements were carried out in a 1 M Na_2SO_4 electrolyte between 0.0 and 1.0 V at various current densities. Figure 7b shows the charge–discharge curves of pristine Mn_3O_4 electrodes. The sloped variation of the charge–discharge curves confirms the pseudocapacitance nature resulting from the redox reaction. However, the IR drop can be found, which is due to the electrical resistance of the Mn_3O_4 and the electrolyte diffusion limitations. The specific capacitances of the electrode can be estimated from the discharge curves according to the equation: $C = I\Delta t/m\Delta V$, where C (F g^{-1}) is the specific capacitance, I (A g^{-1}) is the constant discharging current, Δt (s) is the discharging time, m (g) is the mass of the active material in the working electrode, and ΔV (V) is the potential window. The calculated specific capacitance values of the pristine Mn_3O_4 electrode are 202, 164, 123, 77, 55, and 46 F g^{-1} at current densities of 0.5, 1, 2, 5, 10, and 20 A g^{-1}, respectively.

The CV curves of the doped Mn_3O_4 nanocrystal electrodes are shown in Figure 8. At a low scan rate (10 mV s^{-1}), the CV curves for all electrodes remain symmetrical quasi-rectangular shapes, which also reveals the kinetic reversibility of the redox process as well as the ideal capacitive behaviors. The redox peaks induced by the dopants are hardly found. We can estimate the capacitive behaviors of the Mn_3O_4 electrode by counting the integral charge during the anodic and cathodic scan. Cu- and Ni-doped Mn_3O_4 electrodes exhibit the minimum capacitance, and Cr-doped Mn_3O_4 electrodes exhibit the maximum capacitance. The large Cr- and Ni-doped Mn_3O_4 nanocrystals have different capacitive performances, suggesting

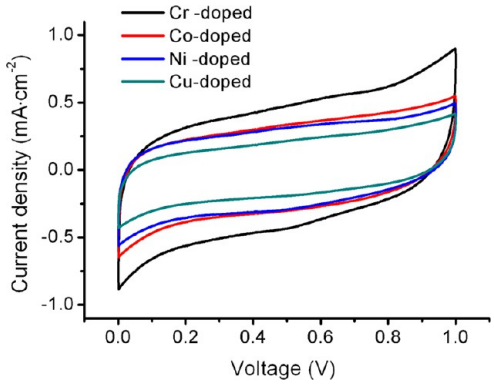

Figure 8. Representative CV curves of doped Mn_3O_4 nanocrystals at a scan rate of 10 mV s^{-1}.

the enhancement in the capacitive performance is mainly due to the type of dopant and is not related to the size effect in the active electrode material. The individual CV results of doped Mn_3O_4 electrodes at various scan rates are shown in Figure S4 (Supporting Information).

The charge–discharge behaviors of the doped Mn_3O_4 electrode are also tested. A decrease of specific capacitance with increasing current densities can be seen in Figure 9. The higher specific capacitance at low current density is due to the sufficient transfer time for ions between the electrolyte and the electrode. In addition, for Cr-doped Mn_3O_4, the situation of the IR drop is improved, which guarantees a better capacitive performance. The specific capacitance values obtained from discharge curves are 272, 209, 184, and 134 F g^{-1} for Cr-, Co-, Ni-, and Cu-doped Mn_3O_4 electrodes at a current density of 0.5 A g^{-1}. The detailed specific capacitances at various current densities are shown in Figure S5 (Supporting Information).

To understand better the possible change of the Mn_3O_4 electrodes before and after doping, electrochemical impedance spectroscopy (EIS) measurements were performed in the same set up as the CV and galvanostatic tests. The Nyquist plots extracted from the EIS of pristine and doped Mn_3O_4 electrodes are shown in Figure 10. In the high-frequency region, the considerably distorted segments with a short length suggest rapid ion transport within the electrode because of its enhanced conductivity by the Ni mesh substrate. In the low-frequency region, the Mn_3O_4 electrodes exhibit a nearly linear branch, indicating a decreased diffusion resistance of the electrolyte ions in the electrode, as expected for a capacitor. The EIS data can be fitted by an equivalent circuit illustrated in the inset of Figure 10.[34,35] The elements in the equivalent circuit include the solution resistance (R_s), the double-layer capacitance (C_{dl}), the charge-transfer resistance (R_{ct}), the Warburg diffusion element (W_o), and the pseudocapacitance element (C_{pseud}). The data of R_s and R_{ct} obtained from the Nyquist plots are listed in Table 1. These results demonstrate the reduced charge-transfer resistance of the Cr-doped Mn_3O_4 electrode. In addition, the long tail at low frequencies of the Cr-doped Mn_3O_4 is closer to a vertical line, also indicating that the Cr-doped Mn_3O_4 has high capacitance and low resistance.

The cycle life performances are of great importance for supercapacitors. The cycling test of the Cr-doped Mn_3O_4 electrode was carried out at 1 A g^{-1} for 1000 cycles. For comparison, the cycle performance of the pristine Mn_3O_4 electrode was also evaluated. The specific capacitances as a function of the cycle numbers are presented in Figure 11. The

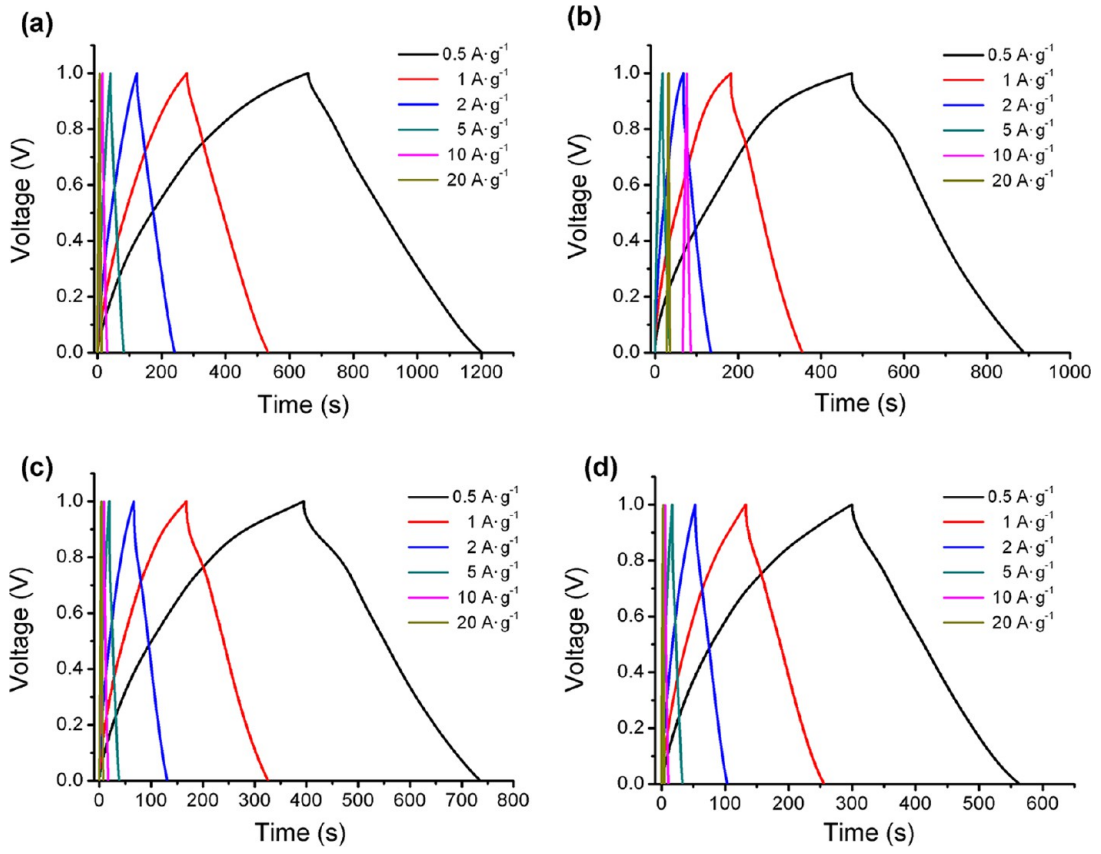

Figure 9. Charge–discharge curves of Cr-doped (a), Co-doped (b), Ni-doped (c), and Cu-doped (d) Mn_3O_4 electrodes.

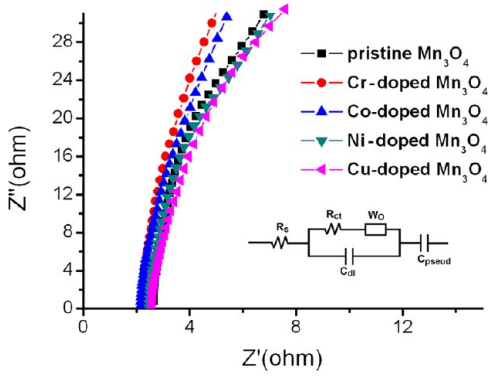

Figure 10. Nyquist plots of pristine and doped Mn_3O_4 electrodes. The inset is the equivalent circuit.

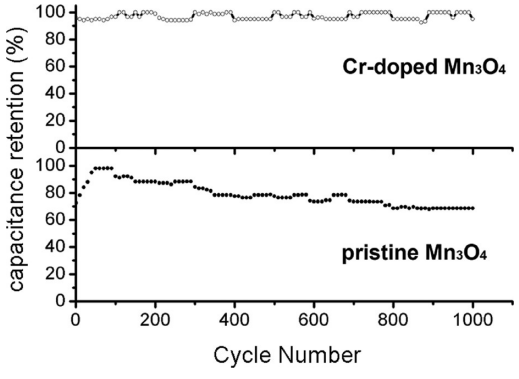

Figure 11. Variations in the capacitance retention of pristine and doped Mn_3O_4 electrodes as a function of the cycle number.

Table 1. Summary of the Impedance Curve Fitting Results of the Mn_3O_4 Electrodes

	R_s (Ω)	R_{ct} (Ω)
Mn_3O_4	2.507	7.842
Cr-doped Mn_3O_4	2.401	6.079
Co-doped Mn_3O_4	2.408	7.038
Ni-doped Mn_3O_4	2.494	7.792
Cu-doped Mn_3O_4	2.457	8.153

results showed pristine and Cr-doped Mn_3O_4 nanocrystals having different cyclic behaviors. For pristine Mn_3O_4 nanocrystals, the specific capacitance increased continuously during the first 50 cycles. However, the degradation in specific capacitance started around 150 cycles. About a 70% capacitance retention compared to the maximum capacitance was observed until 1000 cycles. Meanwhile, for the Cr-doped Mn_3O_4 nanocrystals, during the first 10 cycles, the specific capacitance increased slightly due to the activation effect and was almost maintained at the same value over the following cycles, suggesting an almost 100% capacitance retention and a good long-term electrochemical stability.

For Mn oxide-based supercapacitors, the general charge-storage mechanism have been proposed as an adsorption/desorption (a/d) process at the electrode surface and/or an insertion/extraction (i/e) process in the electrode bulk. The a/d process takes place on the compounds with a high surface area, whereas the i/e process occurs mostly on crystalline Mn oxide compounds. Because of the high degree of crystallinity of the Mn_3O_4 nanocrystals, the i/e process and the strong bulk

dx.doi.org/10.1021/am402257y | ACS Appl. Mater. Interfaces 2013, 5, 9508–9516

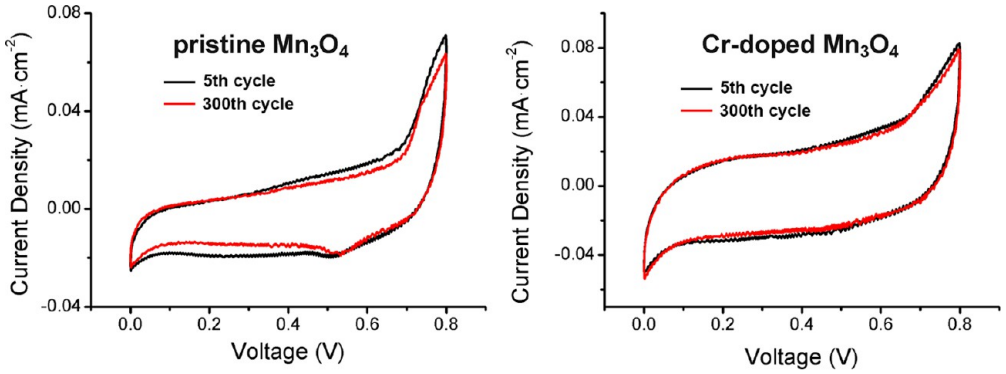

Figure 12. CV curves after the 5th and 300th cycles at a scan rate of 0.5 mV s^{-1} for pristine and Co-doped Mn_3O_4 electrodes.

interaction is expected. However, the capacitive behavior of Mn_3O_4 is regarded as the activation effect of electrochemical cycling. According to previous work, the increased capacitance of Mn_3O_4 nanostructures and a structural transformation of spinel Mn_3O_4 to layered birnessite or stable Mn oxy-hydroxides gradually occurred with the increasing number of the potential cycling in which a pair of redox peaks for the kinetic irreversibility of the redox process are visible in the initial CV curves.[36−38] However, the redox peaks are restricted in the CV curves of the Mn_3O_4-graphene composite electrode, which may due to the fast electron transfer to promote the faradaic process.[39] In the present work, the redox peaks were found to be significant in the CV curves for pristine Mn_3O_4 at low scan rates, and the CV curve showed a significant alteration in shape after cycling 300 times (Figure 12a). However, for doped Mn_3O_4 nanocrystals, the weak redox peaks were insignificant, and the CV curve kept its shape after 300 cycles (Figure 12b). To confirm further the evolution of the Mn oxidation state, Mn_3O_4 nanocrystals before and after cycles were studied by XPS (Supporting Information Figure S6). The binding energy of Mn is significantly different for the two samples. The peak position of Mn $2p_{3/2}$ for Cr-doped sample is still located at 641.7 eV. Meanwhile, the slight peak shift to the higher binding energy (from 641.3 to 642.0 eV) occurs for the pristine sample, suggesting the formation of Mn oxide with higher oxidation state.

Further insights into the evolution occurring in the electrodes can be achieved by EIS patterns (Supporting Information Figure S7). As shown in Figure S7a, the general characteristics of the Nyquist plots for Cr-doped Mn_3O_4 electrode are almost similar before and after cycling. However, for the pristine Mn_3O_4 electrode, the Nyquist plots change obviously at a moderate frequency (Figure S7b). Such change also confirms a structural transformation in the bulk of the electrode because the ac signal can penetrate into the interior of the electrode at a moderate frequency (250−0.1 Hz). Bode plots provide more information about the structural transformation (Figure S7c,d). For the pristine Mn_3O_4 electrode, a dramatic splitting of the impedance occurs at a moderate frequency, whereas the phase angle shifts to a lower frequency. Meanwhile, a stable situation is expected for the doped Mn_3O_4 electrode, suggesting that the phase stability is greatly improved by doping with transition metal, which could be conducive to the practical use of Mn_3O_4 in supercapacitors.

Herein, several transition-metal ions, including Cr, Co, Ni, and Cu, were adopted as dopants. Actually, Ni and Co oxides are proved conclusively to be excellent electrode materials for electrochemical supercapacitors.[40−43] At present, Ni and Co oxides, including their Ni−Co−O composites, were extensively reported to show excellent pseudocapacitive properties that excel over Mn oxides. However, Ni and Co oxides have a narrower operation potential window of approximately 0.5 V. Many research works demonstrated the fabrication of oxide composite electrodes containing a Mn and Ni/Co component.[44−52] Fan et al. reported a synergistic effect using 3D tubular arrays of MnO_2−NiO nanoflakes and hybrid structures of Co_3O_4 nanowire@MnO_2 ultrathin nanosheet core/shell arrays as high-rate supercapacitors electrodes.[51,52] However, such a synergistic effect in the capacitive performance is insignificant for Co-doped Mn_3O_4 even though nanocrystals with a smaller size are achieved, and it is negative for Ni-doped Mn_3O_4. Therefore, the interaction between Mn_3O_4 and dopants or the doping effect on the Mn_3O_4 nanostructures should play a significant role in the improvement of the electrochemical performance. In the present work, each component of the doped Mn_3O_4 nanocrystals electrode is functional: Mn_3O_4 nanocrystals enable the strong bulk interaction within the electrode and provide the main pseudocapacitance and the dopants act in the key role of tuning the phase stability during cycling, facilitating rapid charge transfer and increasing the electrochemical utilization of Mn_3O_4 nanocrystals. These features facilitate the i/e process and electron transport in the electrode, resulting in an enhanced capacitance of doped Mn_3O_4.

4. CONCLUSIONS

The Mn_3O_4 nanocrystals shaped as octahedrons with different sizes are achieved by doping with different transition-metal ions. The phase stability during cycling and the charge-transfer resistance of Mn_3O_4 nanocrystals are obviously improved by Cr doping. The obtained Cr-doped Mn_3O_4 nanocrystals possess a high specific capacitance and excellent cycling stability compared to pristine Mn_3O_4, suggesting a doping effect for the growth and electrochemical performance of mixed-valent Mn oxides. The results in this study may be applied to many mixed-valent oxide materials to improve their electrochemical capacitance by the doping with transition metals. Therefore, this study may provide a new way to improve the capacitive properties of transition-metal oxides for high-performance supercapacitors and batteries.

■ ASSOCIATED CONTENT

Ⓢ Supporting Information

Enlarged XRD patterns, TEM images, EDX spectra, and CV curves of Mn_3O_4 nanocrystals, detailed specific capacitances of

Mn_3O_4 electrodes at various current densities, and XPS and EIS data of Mn_3O_4 electrodes before and after cycles. This material is available free of charge via the Internet at http://pubs.acs.org.

AUTHOR INFORMATION

Corresponding Author

*Tel/Fax: +86-771-3233718. E-mail: fanwang@gxu.edu.cn.

Notes

The authors declare no competing financial interest.

ACKNOWLEDGMENTS

This work was supported by the National Natural Science Foundation of China (grant no. 21163001)

REFERENCES

(1) Zhi, M. J.; Xiang, C. C.; Li, J. T.; Li, M.; Wu, N. Q. *Nanoscale* **2013**, *5*, 72−88.
(2) Wang, G. P.; Zhang, L.; Zhang, J. J. *Chem. Soc. Rev.* **2012**, *41*, 797−828.
(3) Ghodbane, O.; Pascal, J. L.; Favier, F. *ACS Appl. Mater. Interfaces* **2009**, *1*, 1130−1139.
(4) Devaraj, S.; Munichandraiah, N. *J. Phys. Chem. C* **2008**, *112*, 4406−4417.
(5) Toupin, M.; Brousse, T.; Belanger, D. *Chem. Mater.* **2002**, *14*, 3946−3952.
(6) Ghodbane, O.; Ataherian, F.; Wu, N. L.; Favier, F. *J. Power Sources* **2012**, *206*, 454−462.
(7) Song, M. K.; Cheng, S.; Chen, H. Y.; Qin, W. T.; Nam, K. W.; Xu, S. C.; Yang, X. Q.; Bongiorno, A.; Lee, J. S.; Bai, J. M.; Tyson, T. A.; Cho, J.; Liu, M. L. *Nano Lett.* **2012**, *12*, 3483−3490.
(8) Jiang, H.; Zhao, T.; Yan, C. Y.; Ma, J.; Li, C. Z. *Nanoscale* **2010**, *2*, 2195−2198.
(9) Ahmed, K. A. M.; Zeng, Q. M.; Wu, K. B.; Huang, K. X. *J. Solid State Chem.* **2010**, *183*, 744−751.
(10) Dubal, D. P.; Dhawale, D. S.; Salnkhe, R. R.; Fulari, V. J.; Lokhande, C. D. *J. Alloys Compd.* **2010**, *497*, 166−170.
(11) Huang, Y.; Liang, J. J.; Chen, Y. S. *Small* **2012**, *8*, 1805−1834.
(12) Zhai, D. Y.; Li, B. H.; Du, H. D.; Gao, G. Y.; Gan, L.; He, Y. B.; Yang, Q. H.; Kang, F. Y. *Carbon* **2012**, *50*, 5034−5043.
(13) Chang, K. H.; Lee, Y. F.; Hu, C. C.; Chang, C.; Liu, C. L.; Yang, Y. L. *Chem. Commun.* **2010**, *46*, 7957−7959.
(14) Liu, C. L.; Chang, K. H.; Hu, C. C.; Wen, W. C. *J. Power Sources* **2012**, *217*, 184−192.
(15) Lee, J. W.; Hall, A. S.; Kim, J. D.; Mallouk, T. E. *Chem. Mater.* **2012**, *24*, 1158−1164.
(16) Zhang, X.; Sun, X. Z.; Chen, Y.; Zhang, D. C.; Ma, Y. W. *Mater. Lett.* **2012**, *68*, 336−339.
(17) Ma, X.; Chen, H.; Ceder, G. *J. Electrochem. Soc.* **2011**, *158*, A1307−A1312.
(18) Yeager, M.; Du, W. X.; Si, R.; Su, D.; Marinkovic, N.; Teng, X. W. *J. Phys. Chem. C* **2012**, *116*, 20173−20181.
(19) Mai, L. Q.; Li, H.; Zhao, Y. L.; Xu, L.; Xu, X.; Luo, Y. Z.; Zhang, Z. F.; Ke, W.; Niu, C. J.; Zhang, Q. *Sci. Rep.* **2013**, *3*, 1718-1−1718-8.
(20) Li, J. M.; Chang, K. H.; Wu, T. H.; Hu, C. C. *J. Power Sources* **2013**, *224*, 59−65.
(21) Wang, H. L.; Tan, T. A.; Yang, P.; Lai, M. O.; Lu, L. *J. Phys. Chem. C* **2011**, *115*, 6102−6110.
(22) Kang, J. L.; Hirata, A.; Kang, L. J.; Zhang, X. M.; Hou, Y.; Chen, L. Y.; Li, C.; Fujita, T.; Akagi, K.; Chen, M. M. *Angew. Chem., Int. Ed.* **2013**, *52*, 1664−1667.
(23) Ardizzone, S.; Bianchi, C. L.; Tirelli, D. *Colloids Surf., A* **1998**, *134*, 305−312.
(24) Kim, H.; Seo, D. H.; Kim, H. S.; Park, I.; Hong, J. H.; Park, K. Y.; Kang, K. *Chem. Mater.* **2012**, *24*, 720−725.
(25) Na, C. W.; Han, D. S.; Kim, D. S.; Park, J. H.; Jeon, Y. T.; Lee, G. H.; Jung, M. H. *Appl. Phys. Lett.* **2005**, *87*, 142504-1−142504-3.
(26) Zhao, Y.; Li, C. G.; Li, F. F.; Shi, Z.; Feng, S. H. *Dalton Trans.* **2011**, *40*, 583−588.
(27) Wang, C. B.; Yin, L. W.; Xiang, D.; Qi, Y. X. *ACS Appl. Mater. Interfaces* **2012**, *4*, 1636−1642.
(28) Moulder, J. F.; Stickle, W. E.; Sobol, P. E.; Bomben, K. D. *Handbook of X-ray Photoelectron Spectroscopy*; Perkin-Elmer Corp.: Eden Prairie, MN, 1992.
(29) Yang, H. M.; Ouyang, J.; Tang, A. D. *J. Phys. Chem. B* **2007**, *111*, 8006−8013.
(30) Ivill, M.; Pearton, S. J.; Rawal, S.; Leu, L.; Sadik, P.; Das, R.; Hebard, A. F.; Chisholm, M.; Budai, J. D.; Norton, D. P. *New J. Phys.* **2008**, *10*, 065002-1−065002-21.
(31) Fierro, G.; Jacono, M. L.; Inversi, M.; Dragone, R.; Porta, P. *Top. Catal.* **2000**, *10*, 39−48.
(32) Liu, F.; Lee, J. Y.; Zhou, W. J. *Small* **2006**, *2*, 121−128.
(33) Yin, J. Z.; Gao, F.; Wu, Y. F.; Wang, J. Y.; Lu, Q. Y. *CrystEngComm* **2010**, *12*, 3401−3403.
(34) Wu, T. H.; Chu, Y. H.; Hu, C. C.; Hardwick, L. J. *Electrochem. Commun.* **2013**, *27*, 81−84.
(35) Li, X.; Wei, B. Q. *Nano Energy* **2012**, *1*, 479−487.
(36) Dai, Y.; Wang, K.; Xie, J. Y. *Appl. Phys. Lett.* **2007**, *90*, 104102-1−104102-3.
(37) Hu, C. C.; Wu, Y. T.; Chang, K. H. *Chem. Mater.* **2008**, *20*, 2890−2894.
(38) Hua, C. C.; Hung, C. Y.; Chang, K. H.; Yang, Y. L. *J. Power Sources* **2011**, *196*, 847−850.
(39) Lee, J. W.; Hall, A. S.; Kim, J. D.; Mallouk, T. E. *Chem. Mater.* **2012**, *24*, 1158−1164.
(40) Vijayakumar, S.; Nagamuthu, S.; Muralidharan, G. *ACS Appl. Mater. Interfaces* **2013**, *5*, 2188−2196.
(41) Wang, G. P.; Zhang, L.; Zhang, J. J. *Chem. Soc. Rev.* **2012**, *41*, 797−828.
(42) Liu, M. C.; Kong, L. B.; Lu, C.; Li, X. M.; Luo, Y. C.; Kang, L. *ACS Appl. Mater. Interfaces* **2012**, *4*, 4631−4636.
(43) Yuan, C. Z.; Li, J. Y.; Hou, L. R.; Zhang, X. G.; Shen, L. F.; Lou, X. W. *Adv. Funct. Mater.* **2012**, *22*, 4592−4597.
(44) Chang, J. K.; Hsieh, W. C.; Tsai, W. T. *J. Alloys Compd.* **2008**, *461*, 667−674.
(45) Inoue, R.; Nakayama, M. *Electrochem. Solid-State Lett.* **2009**, *12*, A203−A206.
(46) Chen, Y. S.; Hu, C. C. *Electrochem. Solid-State Lett.* **2003**, *6*, A210−A213.
(47) Chuang, P. Y.; Hu, C. C. *Mater. Chem. Phys.* **2005**, *92*, 138−145.
(48) Lin, C. C.; Lee, C. C. *J. Electrochem. Soc.* **2010**, *157*, A230−A236.
(49) Pang, H.; Deng, J. W.; Du, J. M.; Li, S. J.; Li, J.; Ma, Y. H.; Zhang, J. S.; Chen, J. *Dalton Trans.* **2012**, *41*, 10175−10181.
(50) Li, W. Y.; Li, G.; Sun, J. Q.; Zou, R. J.; Xu, K. B.; Sun, Y. G.; Chen, Z. G.; Yang, J. M.; Hu, J. Q. *Nanoscale* **2013**, *5*, 2901−2908.
(51) Liu, J.; Jiang, J.; Bosman, M.; Fan, H. J. *J. Mater. Chem.* **2012**, *22*, 2419−2426.
(52) Liu, J.; Jiang, J.; Cheng, C.; Li, H.; Zhang, J.; Gong, H.; Fan, H. J. *Adv. Mater.* **2011**, *23*, 2076−2081.